scientific reports

Check for updates

OPEN

In vitro biological and antimicrobial properties of chitosan-based bioceramic coatings on zirconium

Salim Levent Aktug[1], Salih Durdu[2], Selin Kalkan[3], Kultigin Cavusoglu[4] & Metin Usta[1,5]✉

Ca-based porous and rough bioceramic surfaces were coated onto zirconium by micro-arc oxidation (MAO). Subsequently, the MAO-coated zirconium surfaces were covered with an antimicrobial chitosan layer via the dip coating method to develop an antimicrobial, bioactive, and biocompatible composite biopolymer and bioceramic layer for implant applications. Cubic ZrO_2, metastable $Ca_{0.15}Zr_{0.85}O_{1.85}$, and $Ca_3(PO_4)_2$ were detected on the MAO surface by powder-XRD. The existence of chitosan on the MAO-coated Zr surfaces was verified by FTIR. The micropores and thermal cracks on the bioceramic MAO surface were sealed using a chitosan coating, where the MAO surface was porous and rough. All elements such as Zr, O, Ca, P, and C were homogenously distributed across both surfaces. Moreover, both surfaces indicated hydrophobic properties. However, the contact angle of the MAO surface was lower than that of the chitosan-based MAO surface. In vitro bioactivity on both surfaces was investigated via XRD, SEM, and EDX analyses post-immersion in simulated body fluid (SBF) for 14 days. In vitro bioactivity was significantly enhanced on the chitosan-based MAO surface with respect to the MAO surface. In vitro microbial adhesions on the chitosan-based MAO surfaces were lower than the MAO surfaces for *Staphylococcus aureus* and *Escherichia coli*.

The amount of zirconium that exists in the body is only 1 mg in total on average, and does not have a natural biological role in the human body[1]. Zirconium can be a potential candidate for surgical implant material due to its promising properties such as low Young's Modulus (92 GPa) and excellent biocompatibility compared to titanium and its alloys[2–4]. However, zirconium cannot directly bond to bone tissue at an early stage after implantation due to its bioinert nature[5,6]. Moreover, the microbial property of zirconium may cause postoperative infection[7–9]. It is clear that one of the major problems with the implant surfaces is microbial colonization, whereas their bioactivity and biocompatibility are improved[10–12]. Thus, zirconium has limited medical applications. In order to overcome this disadvantage, it is vital to enhance the bioactivity and antimicrobial properties via surface treatment.

Micro-arc oxidation (MAO) enhances bioactivity, biocompatibility, and corrosion resistance[2,5,13,14]. MAO that can form porous, thick, relatively rough, and firmly adherent oxide coatings on zirconium surfaces represents a promising electrochemical coating technique[2,5,15,16]. MAO, which produces bioactive and biocompatible ceramic coatings, involves anodic oxidation in aqueous electrolytes above the dielectric breakdown voltage. The short-lived micro-discharges occur locally at weak sites that are susceptible to dielectric breakdown under the high temperatures and pressures associated with the MAO process[17,18]. Eventually, porous and rough bioceramic surfaces form on metal surfaces. The properties of the MAO coatings depend on certain experimental parameters such as the substrate, the electrolyte, voltage, current, and the treatment time[19].

Antibiotics could be presented to the implant surface to reduce the risk of postoperative infection by preventing microbial adhesion and proliferation[20,21]. However, antibiotic resistance is an important problem that requires primary clinical attention[22]. It is well known that many important pathogens, *S. aureus* being prime among them, always exhibit highly alarming levels of antibiotic resistance[23,24]. Furthermore, bacteria forming biofilms on prosthetic surfaces are resistant to antimicrobials[25–27]. Thus, instead of antibiotics, biopolymer chitosan is preferred due to its antimicrobial properties[28].

Chitosan is a critical antimicrobial agent that has been widely investigated in recent years[29,30]. Chitosan is a natural polysaccharide obtained from deacetylation of chitin, which is found in the exoskeletons of crustaceans and insects, and in certain fungi and microorganisms[31]. This biopolymer exhibits excellent features due to its nontoxic nature, biodegradability, and promoting cell adhesion. The importance of the antimicrobial properties

[1]Materials Science and Engineering, Gebze Technical University, 41400 Gebze, Turkey. [2]Industrial Engineering, Giresun University, 28200 Giresun, Turkey. [3]Bioprocess Engineering, Giresun University, 28200 Giresun, Turkey. [4]Department of Biology, Giresun University, 28200 Giresun, Turkey. [5]Materials Institute, TUBITAK Marmara Research Center, 41470 Gebze, Turkey. ✉email: ustam@gtu.edu.tr

of chitosan can be explained by the electrostatic interaction between chitosan and microbial cells[32–34]. Chitosan is a positively charged polymer and the protonated amino group of chitosan is available to bind to the negatively charged microbial cell wall. Moreover, it disrupts mass transport across the cell wall, accelerating the death of bacteria[33,35,36]. The disruption of the bacterial membrane also leads to inhibition of the DNA-membrane complex, which has an important role in chromosome segregation, replication, transcription, or the maintenance of the physical configuration of the DNA[37,38]. Thus, natural biopolymer chitosan is proposed as an important antibacterial agent on the MAO-coated zirconium surfaces in this work.

Usually, the chitosan layer has been deposited on the MAO-coated magnesium and titanium metal surfaces in the literature, though some research has been carried out on the fabrication and investigation of properties of chitosan-based MAO surfaces on titanium and magnesium[29,39–46]. Wang et al. investigated micro-RNA-21-loaded chitosan and hyaluronic acid nanoparticles on MAO titanium surfaces[39]. Neupane et al. fabricated chitosan coating on MAO-coated Ti surfaces modified via hydrothermal treatment[40]. Fang et al. investigated the immobilization of chitosan film containing semaphorin 3A on a MAO-coated titanium surface via the silane reaction to improve MG63 osteogenic differentiation[41]. Cheng et al. studied the deposition of cefazolin sodium/chitosan composite film on MAO coatings containing Si, Ca, and Na on titanium[44]. Li et al. investigated the biological and antibacterial properties of the micro- and nanostructured hydroxyapatite/chitosan coating on titanium[29]. Micropores were sealed by the formation of chitosan on the bioceramic MAO-coated titanium and magnesium surface. However, to our knowledge there has been no previous study on the fabrication and investigation of an antimicrobial chitosan-based biopolymer structure on MAO-coated Zr surfaces to date.

In our previous work, antimicrobial Ag, Cu, and Zn-based nanolayers were produced on MAO-coated Zr surfaces, and their biological properties were investigated in detail[7–9]. In this work, natural chitosan-based MAO coatings with antimicrobial and bioactive properties were produced on Zr metal for the first time in the literature. Firstly, porous and bioactive Ca-based bioceramic surfaces were used to coat Zr metal via the MAO technique. Following the MAO, an antimicrobial chitosan layer was applied to form a uniform coating on the MAO surface. The phase structure, functional groups, surface morphologies, elemental distributions, and hydrophilic/hydrophobic properties of all coatings were analysed via XRD, FTIR, SEM, EDX-mapping, and contact angle measurements. In addition, in vitro predictions of bioactivity under bodily conditions and antimicrobial properties for gram-positive (*Staphylococcus aureus*) and gram-negative (*Escherichia coli*) bacteria of both coatings were investigated. Finally, both coatings were compared with each other in detail.

Experimental details

Sample preparation. Commercial pure zirconium (Zr 702) plates were used as the metal substrates for the MAO process. Initially, the substrates were cut into pieces to a size of 30 mm × 25 mm × 5 mm. Then, the substrates were ground using 400#, 800# and 1200# SiC sandpapers. Finally, they were cleaned in acetone in an ultrasonic bath dried under warm air by a heat gun.

MAO coating production. In this study, the MAO device (MDO-100WS-100 kW), which operated from an AC (alternating current) power supply was used as preferred in our previous studies[7–9,47,48]. The Zr substrates served as an anode (working electrode) and the stainless-steel container served as a cathode in the MAO process. The MAO electrolyte consisted of 0.25 M calcium acetate and 0.06 M β-calcium glycerophosphate. The electrolyte was prepared by dissolving of all chemicals in deionized water[7–9,47,48]. The MAO treatment was carried out at 0.292 A/cm^2 for 10 min. The electrolyte temperature was not allowed to exceed 40 °C during the MAO process via a water-cooling circulator system. After the MAO treatment, they were dried using hot air and preserved in a desiccator.

Preparation of chitosan solution and coating. The medium molecular weight chitosan used to prepare solutions was purchased from Sigma-Aldrich, Milwaukee. According to the manufacturer (Sigma-Aldrich, Milwaukee), the molecular weight, viscosity, the degree of deacetylation and polydispersity of medium molecular weight chitosan are as 20 kDa, 200–800 cp, 75–85% and 7.3 Mw/Mn, respectively. The chitosan was dissolved in 1.0 wt% aqueous acetic acid solution with concentrations of 1.0 vol%. The solution was stirred for 1 h until the chitosan was completely dissolved at room temperature. The MAO samples were dipped into the chitosan solution for 5 min. The then chitosan-coated MAO samples were drawn out at a constant rate and were dried at 37 °C. This procedure was repeated three times to ensure the solution covered both the micropores and thermal cracks in the MAO coating. Finally, to prevent thermal stresses, the chitosan-coated MAO samples were dried in atmosphere at room temperature for 24 h[45]. Thus, free chitosan used without rinsing might be the source of the antibacterial after dipping process.

Surface characterization. The phase structures of the MAO coating surfaces were identified using a powder XRD device (XRD: Bruker D8 Advance) with Cu-Kα radiation at a scanning speed of 1° min^{-1} between 20° and 80°. The chitosan-based MAO coating was probed by using ATR FT IR device (FT IR: JASCO FT/IR 6600) in the wavenumber range from 4000 to 400 cm^{-1}. The surface morphologies of both surfaces were determined via SEM (SEM: Hitachi SU1510). The EDX attached to the SEM was used to analyse elemental composition and amounts in both surfaces. The average contact angles were determined using a contact angle goniometer (CAG: Dataphysics OCA 15EC). The CAG device was used with a sessile drop technique through all analyses. The average contact angle measurements were carried out within 60 s using the SCA software after touching a 1 µL drop of distilled water onto both coating surfaces.

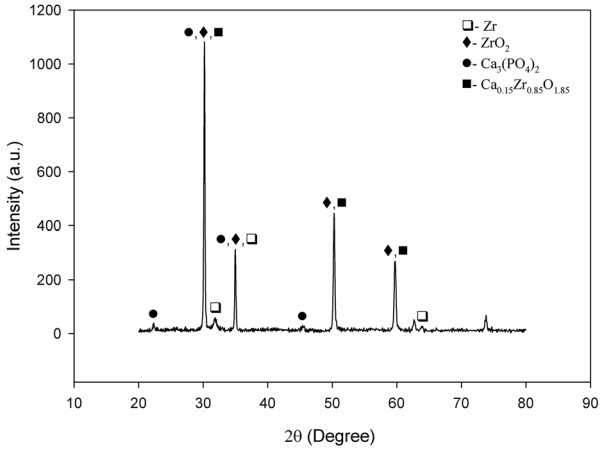

Figure 1. XRD spectra of the MAO coating.

Bioactivity properties. In vitro predictions of bioactivity for both coatings were evaluated by immersion test in simulated body fluid (SBF). For this experiment, Kokubo and Takadama's SBF recipe (1.0 × SBF) was used[49]. Both coatings were immersed for 14 days at 36.5 °C, with the SBF being refreshed every two days. The SBF was prepared by dissolving reagent-grade NaCl, $NaHCO_3$, KCl, $K_2HPO_4{\cdot}3H_2O$, $MgCl_2{\cdot}6H_2O$, $CaCl_2$, and Na_2SO_4 into deionized water and buffering to pH 7.40 with $(CH_2OH)_3CNH_2$ and 1.0 M HCl at 36.5 °C. The surface area ratio of the coating surfaces with respect to the SBF volume was set to be approximately equal to 10[49]. Both coatings were gently washed in distilled water post-immersion in SBF. Finally, they were allowed to dry at room temperature and then transferred into desiccators.

Post-immersion in SBF, both coatings were analysed via XRD, SEM, EDX-mapping, and EDX-area. The phase structures of each of the immersed surfaces were investigated via XRD (GNR Europe 600) with Cu-Kα radiation at a scanning speed of 1° min^{-1} from 20° to 80°. The surface morphology of each of the immersed surfaces were analysed via SEM (Hitachi SU1510) up to magnification of 10,000×. The elemental distribution and elemental amount on each of the immersed surfaces were investigated via EDX-mapping and EDX-area analysis.

Antimicrobial properties. The antimicrobial properties of the uncoated and chitosan-coated surfaces were determined via agar diffusion test. The antimicrobial activity of the surfaces was tested against a gram-negative bacterium such as *Escherichia coli* ATCC 11293 and a gram-positive bacterium such as *Staphylococcus aureus* ATCC 6538. For this purpose, fresh bacterial broth was prepared from stock cultures. The bacterial cultures to be used in the agar diffusion test were prepared from the fresh medium of each strain according to McFarland 1.0 standards (10^9 CFU). 100 µL of the prepared suspension was homogeneously spread over the surface of Müller Hinton Agar. The MAO and chitosan-coated MAO surfaces were placed in Petri dishes and incubated at 37 °C for 24 h. The diameters of the inhibition zones (mm) formed around the coating were evaluated for antimicrobial properties. Tetracycline and ceftazidime were used as positive controls for *E. coli* and *S. aureus*, respectively, and all tests were repeated in triplicate.

Statistical analysis. Statistical analysis was performed using the "IBM SPSS Statistics 22 SP" program suite. Data were reported as mean ± SD (standard deviation). The statistical significance between the means was determined via one-way ANOVA and Duncan's test, with $p < 0.05$ considered statistically significant.

Results and discussion

The phase structure of the MAO coating was investigated via powder XRD analyses, as shown in Fig. 1. As seen in the resultant XRD spectra, the phases of Zr, cubic ZrO_2, metastable $Ca_{0.15}Zr_{0.85}O_{1.85}$, and $Ca_3(PO_4)_2$ were detected on the MAO surface. Cubic ZrO_2 and $Ca_3(PO_4)_2$ were observed as the major phases, while Zr was found as a minor phase in the coating structure. The Zr signal in the XRD spectra derives from the substrate and metallic compounds on the coating. Firstly, the ZrO_2 was formed by the reaction of oppositely charged Zr^{4+} and OH^- ions at high pressure and temperature due to the micro-discharge channels present in the initial steps of MAO. The instant localized temperature in the micro-discharge channels can reach up to 2500 K, as reported in the literature[50]. Therefore, stable cubic ZrO_2 was observed throughout the entire surface. Moreover, the ZrO_2 phase, which serves as nucleation sites, contributed to the formation of Ca-based phases such as $Ca_3(PO_4)_2$, $Ca_{0.15}Zr_{0.85}O_{1.85}$, and $Ca_{10}(PO_4)_6(OH)_2$[47,48]. Positively charged Ca^{2+} and negatively charged PO_4^{3-} ions derived from the electrolyte reacted with each other on the ZrO_2–based micro-discharge channels. $Ca_3(PO_4)_2$ was then formed on the MAO surface. Simultaneously, the Zr^{4+} from the substrate and the Ca^{2+} and OH^- from the electrolyte combined with each other on the micro-discharge channels, subsequently forming metastable $Ca_{0.15}Zr_{0.85}O_{1.85}$[51].

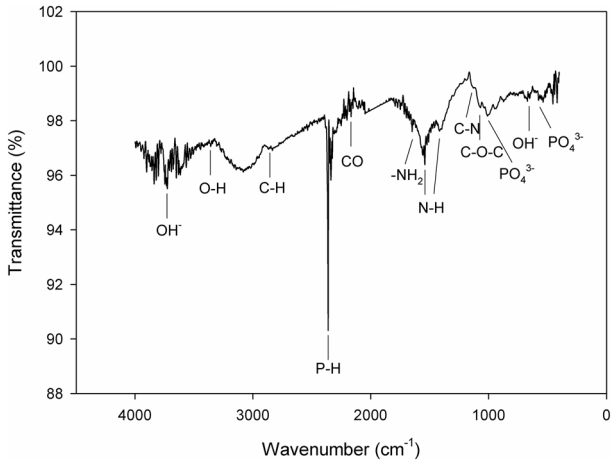

Figure 2. FTIR spectra of the chitosan-based MAO coating.

The FT-IR spectra of the chitosan-based MAO coatings are shown in Fig. 2, where the characteristic bands of chitosan, ZrO_2, and calcium apatite-based structures can be observed. The FTIR peaks located at 560–570, 645–655, 1028, 1089, 1150, 1425, 1590, 1657, 2140–2165, 2340–2380, 2872, 3360–3370, and 3730–3750 cm^{-1} correspond to various vibrational modes characteristically associated with PO_4^{3-}, OH–, PO_4^{3-}, C–O–C, C–N, N–H, N–H, $–NH_2$, CO, P–H, C–H, O–H, and OH^- species, respectively[46,51–59]. Two peaks located at 1089 and 1150 cm^{-1} are the characteristic absorption peaks of the C–O–C and C–N stretching modes, respectively[46,57]. The absorption band peaks at 1425 and 1590 cm^{-1} correspond to the N–H band[46,56,57]. The stretching peak at 1657 cm^{-1} corresponds to $–NH_2$[46]. The stretching vibration band peaks at 2872 cm^{-1} can be attributed to the C–H in methyl or methenyl functional groups[46]. The stretching vibrations of non-associated peaks at 3360–3370 cm^{-1} correspond to an O–H band[58]. All of these peaks verify the existence of a chitosan-based layer structure on the MAO surface[46]. Furthermore, the other peaks support the presence of cubic ZrO_2, $Ca_3(PO_4)_2$, and apatite. The characteristic band peak at 1028 cm^{-1} verifies the existence of $Ca_3(PO_4)_2$[59]. The absorption band peak at 2140–2165 cm^{-1} verifies the existence of c-ZrO_2[51]. The stretching vibration, libration-deformation, stretching vibration, and stretching vibration band peaks at 560–570, 645–655, 2340–2380 and 3730–3750 cm^{-1} are characteristic of the existence of apatite[51–55]. However, crystalline apatite was not observed on the MAO surfaces by XRD, as can be seen in Fig. 1. Thus, it could be concluded that the MAO coatings contained an amorphous apatite structure because it could not be kinetically transformed to the crystalline form during the MAO process.

The surface morphologies of the MAO and chitosan-based MAO coatings were investigated via SEM, as can be seen in Fig. 3. The surface of the MAO coatings was highly porous and rough owing to the presence of micro-sparks during the MAO process. A large number of micropores and voids were found on the MAO surface. Cracks were found on the MAO surface because the thermal stresses between the highly localized hot surface and cold electrolyte during the process. It is well known that these types of porous and rough bioceramic surfaces are beneficial to cell attachment, proliferation, and tissue growth under bodily conditions for biomedical implant applications. All pores and voids were filled with the antimicrobial type of chitosan polymer structure when the MAO surface was dip coated, after which the homogeneous antimicrobial chitosan-based MAO surfaces were fabricated on zirconium. After being coated with a chitosan layer on the MAO surface, any micropores, voids and thermal cracks were not observed as shown in Fig. 3b. This suggests that chitosan-coated MAO surfaces were completely covered. The newly formed chitosan-based layered were observed on the surface. Spherical structures were locally observed on the MAO surface at low magnifications. It is well known that chitosan precipitates at pH 7.4[60]. A new layer formed on the MAO surface is generally non-spherical as seen in Fig. 3b.

The elemental distribution on both surfaces were analysed via EDX-mapping, as illustrated in Fig. 4. The elemental analysis for each surface are given in Table 1. As expected, only Ca, P, O, and Zr were detected on the MAO surface. The Ca, P, and O originated from the calcium acetate- and calcium glycerophosphate-based electrolyte, with Zr coming from the metallic substrate, as expected. Furthermore, all detected elements were homogenously distributed across the entire MAO surface, as shown in Fig. 4a. Besides the existence of Ca, P, and O, C was detected on the chitosan-based MAO surface. This element was uniformly dispersed across the surface on the post-coating chitosan layer. The chitosan structures naturally contain C and O; however, no Zr was observed on the chitosan-based MAO surface. It was concluded that the Zr-based oxide structures found on the inner layer and the outer surface mainly consisted of Ca-based bioactive and biocompatible elements and phase structures. This clearly supports the premise of the contribution of ZrO_2 to the formation of Ca-based structures.

The wettability of both surfaces was investigated by a sessile drop-contact angle measurement technique, as shown in Fig. 5. The average contact angles of the MAO and chitosan-based MAO surfaces were measured as 94.0° ± 0.3 and 113.5° ± 0.2, respectively. All measurements were repeated three times to get an average value of the wettability of the surfaces. Both surfaces had hydrophobic properties since the average contact angle values were greater than 90°. However, in terms of compassion, the chitosan-based MAO surface indicated the hydrophobic character of the MAO surface. Wettability mainly depends on the morphological structures/chemical

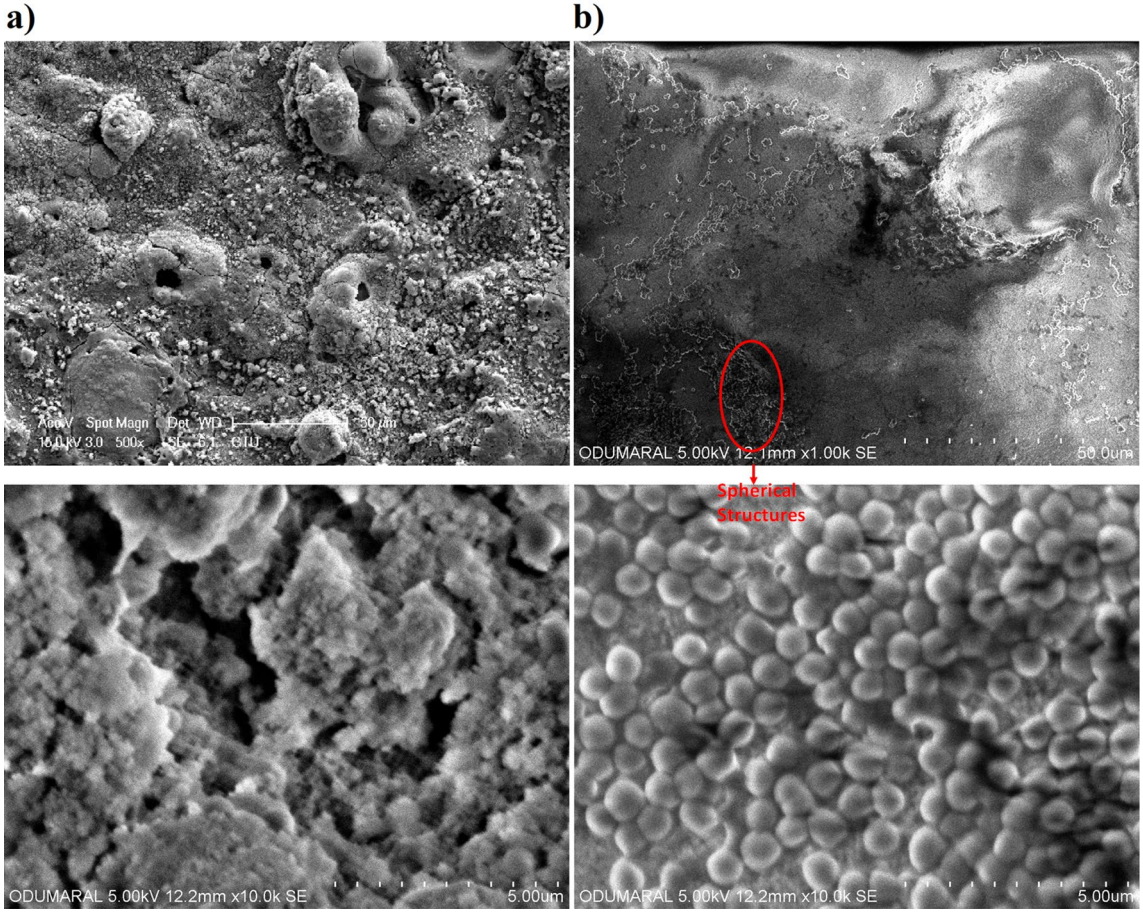

Figure 3. SEM images of the coatings with low and high magnifications: (**a**) the MAO and (**b**) chitosan-based MAO surfaces.

composition of a given surface. The MAO surfaces, which had large numbers of voids and thermal cracks, were porous structures, as can be observed in Fig. 3a. The MAO surfaces usually exhibit hydrophilic properties owing to the capillary effect on the liquid due to the pores[61]. Thus, the water droplet on the MAO surface will be easily absorbed and spread compared to the more homogenous chitosan-based biopolymer surface. The highest initial contact angle was in agreement for the chitosan-coated substrate to the value reported in the literature, which can be attributed to the basis of its chemical properties[62]. The large initial contact angle observed might indicate the reorganization of the molecule which is presumably associated with the methyl moieties of the residual acetyl groups along the polysaccharide backbone[63]. Therefore, the wettability of the chitosan-based MAO surface was lower than that of the MAO surface.

In vitro immersion tests of the MAO and chitosan-based MAO surfaces were carried out at 36.5 °C in SBF for 14 days. It is well known that this test gives information that allows for the prediction of surface bioactivity. Post-immersion in SBF, the phase structure, surface morphology, and elemental distribution of each surface were analysed via XRD (Fig. 6), SEM (Fig. 7), and EDX-mapping (Fig. 8). Moreover, the amount of each element that had formed on each of the surfaces post-immersion in SBF is given in Table 2. As seen in Fig. 6, a TCP ($Ca_3(PO_4)_2$) and a hydroxyapatite ($Ca_5(PO_4)_3(OH)$) structure were detected as major phases on both surfaces. The Ca^{2+} ions, which were released from the proteins, adsorb PO_4^{3-} ions by electrostatic interactions in the SBF solution[64]. They then simultaneously react with each other to form $Ca_3(PO_4)_2$ during the early stages of immersion in SBF. Finally, they react with OH^- ions and transform to $Ca_5(PO_4)_3(OH)$ through the immersion process. The mechanism by which the hydroxyapatite structure formed on different surface types such as undoped and antimicrobial Ag-, Cu-, and Zn-doped MAO surfaces post-immersion in SBF have been discussed in detail in our previous studies[7–9,47,48]. The SBF immersion test revealed that the chitosan layer was favourable for hydroxyapatite formation. The bioactivity of chitosan originated due to the large number of protonated amino groups on the chitosan surface. Chitosan's surface can absorb OH^- ions in SBF via hydrogen bonding and electrostatic attraction. Eventually, they would be adsorbed by the Ca^{2+} and PO_4^{3-} in solution via electrostatic attraction. Finally, their reaction under SBF conditions forms the bone-like apatite on the chitosan-based MAO surface[29]. Furthermore, the chitosan layer contributes to the nucleation of hydroxyapatite because it contains a large amount of OH^-[65]. The original porous bioceramic MAO and nonporous biopolymeric chitosan-based MAO surfaces were filled with a new secondary apatite layer post immersion in SBF. As shown in Fig. 7, the new homogeneous apatite layer formed was deposit across the entirety of both surface layers. There are some cracks in Fig. 7a with respect to Fig. 7b. The top layers of both surfaces are dissolved during immersion in SBF. Thus, micro-cracks

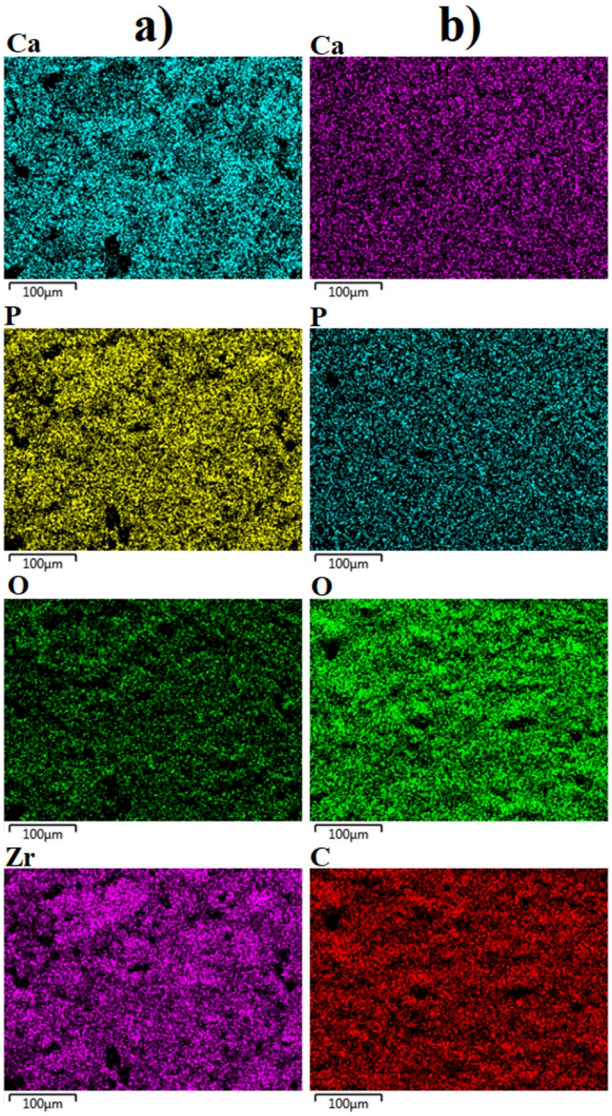

Figure 4. EDX-mapping analysis images of the coatings: (**a**) the MAO and (**b**) chitosan-based MAO surfaces.

	MAO coating		Chitosan-based MAO coating	
Elements	wt%	at%	wt%	at%
Zr	23.72	6.81	–	–
O	42.14	69.04	49.03	46.36
Ca	24.68	16.14	8.09	3.05
P	9.46	8.00	4.29	2.09
C	–	–	38.45	48.42

Table 1. EDS spectra results of the MAO and chitosan-based MAO coatings.

are observed on new apatite layers on both surfaces post-immersion. The dissolved layer on the surfaces may present micro-cracks in the coatings or may propagate micro-cracks on the surface as part of the post-immersion process due to the presence of residual stresses being released[66]. However, the micro-cracks that occurred on the chitosan-based MAO surface were smaller and thinner than those on the plain MAO surface. The Ca, P, and O are necessary basic elements for the formation of apatite. Only, Ca, P, and O were observed on each surface post immersion in SBF. Furthermore, they were uniformly distributed across the whole surface, as shown in Fig. 8. Furthermore, the amount of each element of each of the surfaces post-immersion in SBF were the similar to the

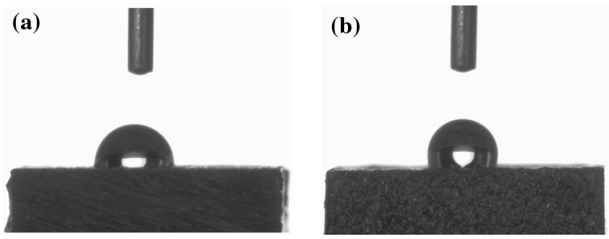

Figure 5. The representative images of droplets contacted on the coatings for 60 s (**a**) the MAO and (**b**) chitosan-based MAO surfaces.

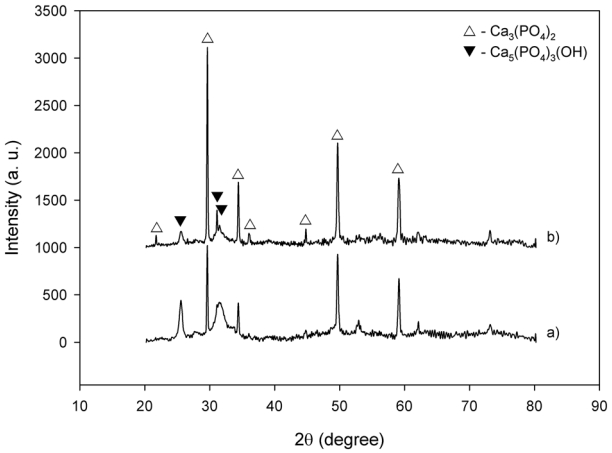

Figure 6. XRD spectra of the coatings at post-immersion in SBF: (**a**) the MAO and (**b**) chitosan-based MAO surfaces.

values reported in Table 2. As shown in Table 2, the amounts of each element, namely Ca, P, and O, detected on each of the surfaces were nearly identical. Therefore, no negative effect on the bioactivity of the chitosan-layer on the MAO surface. Moreover, these results confirmed that both coatings showed excellent bioactivity.

The antimicrobial activities of MAO and chitosan-coated MAO surfaces were examined via the agar diffusion test, the results of which are given in Fig. 9a–c. The minimum inhibition zone for both strains was obtained with the MAO surfaces. The MAO surface exhibited 5.5 ± 0.7 and 4.2 ± 0.3 mm inhibition zones against *E. coli* and *S. aureus*, respectively. It was observed that after the chitosan coating of the surface, the inhibition zones obtained against bacteria increased significantly ($p < 0.05$). Chitosan-based MAO surfaces exhibited 21.6 ± 1.3 and 13.7 ± 0.9 mm inhibition zones against *E. coli* and *S. aureus*, respectively. It was determined that chitosan-based MAO surfaces have 74.5% greater antimicrobial activity against *E. coli* than MAO surfaces. For *S. aureus*, chitosan-based MAO surfaces exhibited 69.3% more antimicrobial activity than the MAO counterparts. This result can be related to the antimicrobial properties of the chitosan coating. Free chitosan used without rinsed might be the source of the antibacterial after dipping process. Chitosan is the deacetylation product of the chitin molecule. Chitin is a linear biopolymer formed by the bonding of *N*-acetyl D-glucosamine units via glycosidic bonds[67]. Chitin is insoluble in many solvents due to its compact structure. The lack of solubility in dilute acid or alkaline solvents, and especially in water, limits chitin's usability[68]. In order to increase its solubility and usability, chitin is subjected to deacetylation with NaOH from which high solubility chitosan is formed. Chitosan is a straight-chain polymer consisting of D-glucosamine and *N*-acetyl D-glucosamine[69]. It contains a large number of amine groups and is thus easily soluble in acidic solutions. Chitosan, which is physically, chemically, and biologically compatible, is known to have medical activities such as being antidiabetic, antimicrobial, antioxidant, and antitumor[70]. The antimicrobial activity of chitosan is due to its polycationic structure[71]. Positively charged chitosan interacts with the negatively charged components of the bacterial cell causing disruptions in normal cell metabolism[72]. It is reported in the literature that many materials coated with chitosan exhibit different levels of antimicrobial properties. Zhang et al. reported that chitosan-TiO_2 composite materials exhibit strong antimicrobial activity against *E. coli*, *S. aureus*, *C. albicans* and *A. niger*[73]. In another study, Munteanu et al. found that chitosan-coated polyethylene surfaces provided 100% inhibition against *S. enteritidis* after 48 h of interaction, while providing 96.43% inhibition against *E. coli* [74].

Another important result obtained from the antimicrobial test is that chitosan-coated MAO surfaces have a greater effect against *E. coli* than *S. aureus*. This result shows that, in general, the chitosan-coated MAO surface is more effective against gram-negative than gram-positive bacteria. It was determined that the antimicrobial effectiveness of chitosan-coated MAO surfaces against *E. coli* is 1.58 times greater than against *S. aureus*. This

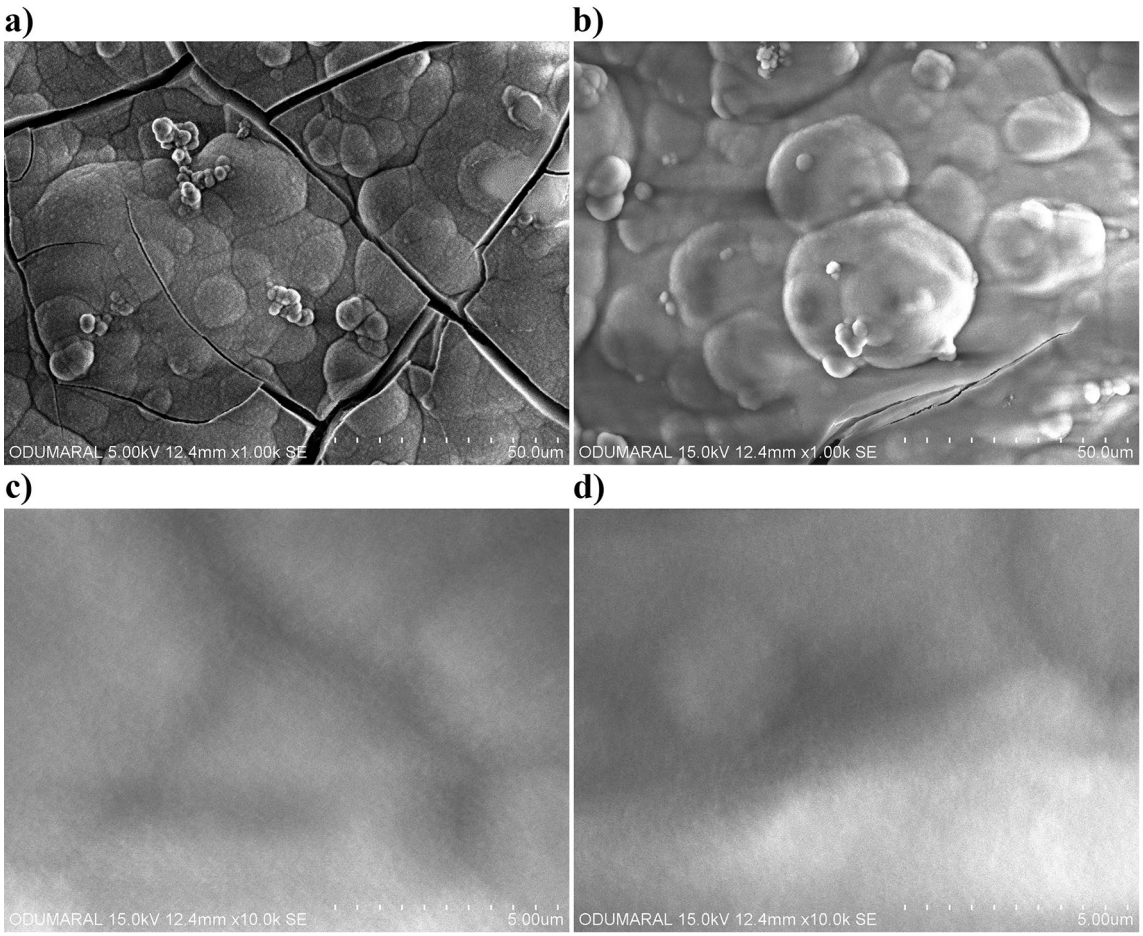

Figure 7. The surface morphologies of the coatings immersed in SBF for 14 days: (**a**,**c**) for the MAO and (**b**,**d**) for chitosan-based MAO surfaces.

result can be explained by the differences in the cellular structure of gram-positive and gram-negative bacteria. The fact that the gram-negative bacteria surface has more hydrophilic character compared to gram-positive bacteria makes them more susceptible to chitosan[75]. This higher hydrophilic property leads to greater interaction with chitosan and large changes in the structure and permeability of the cell membrane. These alterations result in bactericidal effects and bacterial death[76]. Similar studies have demonstrated that chitosan-coated surfaces have a higher inhibitory effect against gram-negative bacteria. Munteanu et al. examined the inhibitory effect of chitosan-coated films with two gram-negative bacteria, namely *S. enteritidis* and *E. coli*, and a gram-positive bacteria, *L. monocytogenes*, and reported high inhibition in gram-negatives[74]. Esmaeili et al. reported that chitosan-coated nanoparticles exhibited significant antimicrobial effect against gram-negative bacteria[77]. As a result, it was determined that chitosan-based MAO surfaces have high antimicrobial properties compared to the MAO surfaces and exhibit broad-spectrum activity that affects both gram-negative and gram-positive bacteria.

Conclusions

In this work, antimicrobial and bioactive chitosan-based MAO biopolymer and bioceramic composite surfaces were fabricated on commercial pure Zr by MAO and dip-coating methods. The chitosan-based MAO surface was observed to be nonporous and crack-free post-fabrication dip coating, while the MAO surface was porous and rough due to the existence of micro-sparks during the process. All elements such as C, Zr, Ca, P, and O, which contributed to form antimicrobial, bioactive, and biocompatible phases, were homogeneously separated during the surfaces. The chitosan-based MAO surface indicated hydrophobic character with respect to the MAO surface because the chemical composition was changed, and the porous surface was eliminated. In vitro prediction of bioactivity and the apatite-forming abilities of the chitosan-based MAO surfaces were considerably improved compared to the plain MAO surfaces. Furthermore, bacterial adhesion to the chitosan-based MAO surfaces was less than that of plain MAO surfaces for *E. coli* and *S. aureus*.

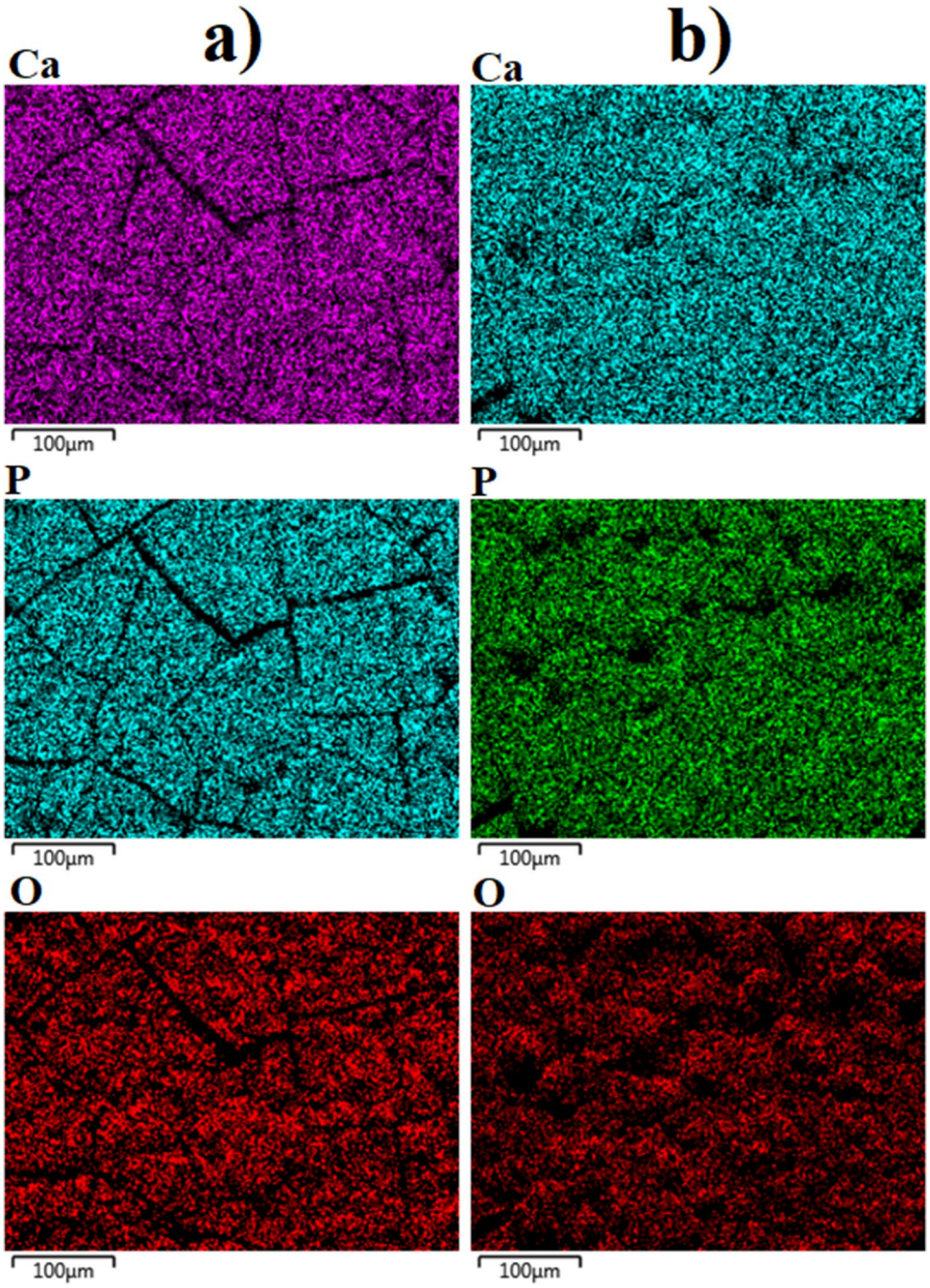

Figure 8. EDX-mapping analysis images of the coatings at post-immersion in SBF: (**a**) the MAO and (**b**) chitosan-based MAO surfaces.

Elements	MAO coating		Chitosan-based MAO coating	
	wt%	at%	wt%	at%
Ca	33.23	18.62	33.32	18.69
P	18.19	13.19	18.18	13.19
O	48.57	68.19	48.49	68.12

Table 2. EDS spectra results of the MAO and chitosan-based MAO coatings at post-immersion in SBF.

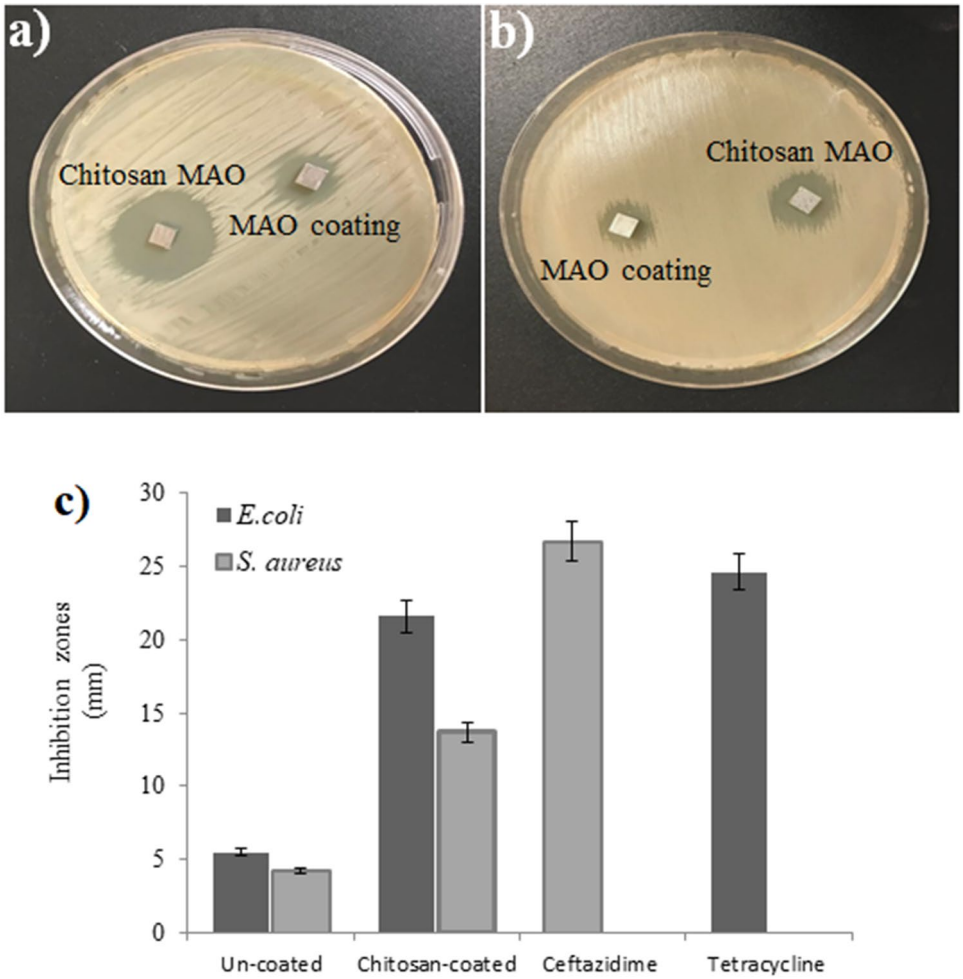

Figure 9. Inhibition zones of the MAO and chitosan-based MAO coated surfaces (**a**) *E. coli*, and (**b**) *S. aureus* and (**c**) inhibition zones (mm) of the MAO and chitosan-based MAO surfaces.

Received: 4 February 2021; Accepted: 13 July 2021
Published online: 23 July 2021

References

1. Chen, Q. Z. & Thouas, G. A. Metallic implant biomaterials. *Mater. Sci. Eng. R Rep.* **87**, 1–57. https://doi.org/10.1016/j.mser.2014.10.001 (2015).
2. Yan, Y. Y. & Han, Y. Structure and bioactivity of micro-arc oxidized zirconia films. *Surf. Coat. Technol.* **201**, 5692–5695. https://doi.org/10.1016/j.surfcoat.2006.07.058 (2007).
3. Johansson, C. B., Wennerberg, A. & Albrektsson, T. Quantitative comparison of screw-shaped commercially pure titanium and zirconium implants in rabbit tibia. *J. Mater. Sci. Mater. Med.* **5**, 340–344. https://doi.org/10.1007/bf00058959 (1994).
4. Thomsen, P. *et al.* Structure of the interface between rabbit cortical bone and implants of gold, zirconium and titanium. *J. Mater. Sci. Mater. Med.* **8**, 653–665. https://doi.org/10.1023/a:1018579605426 (1997).
5. Ha, J. Y. *et al.* Enhancement of calcium phosphate formation on zirconium by micro-arc oxidation and chemical treatments. *Surf. Coat. Technol.* **205**, 4948–4955. https://doi.org/10.1016/j.surfcoat.2011.04.079 (2011).
6. Sharkeev, Y. *et al.* Analyzing the deformation and fracture of bioinert titanium, zirconium and niobium alloys in different structural states by the use of infrared thermography. *Metals* **8**, 703. https://doi.org/10.3390/met8090703 (2018).
7. Aktug, S. L., Durdu, S., Aktas, S., Yalcin, E. & Usta, M. Characterization and investigation of in vitro properties of antibacterial copper deposited on bioactive ZrO_2 coatings on zirconium. *Thin Solid Films* **681**, 69–77. https://doi.org/10.1016/j.tsf.2019.04.042 (2019).
8. Durdu, S., Aktug, S. L., Aktas, S., Yalcin, E. & Usta, M. Fabrication and in vitro properties of zinc-based superhydrophilic bioceramic coatings on zirconium. *Surf. Coat. Technol.* **344**, 467–478. https://doi.org/10.1016/j.surfcoat.2018.03.062 (2018).
9. Durdu, S. *et al.* Characterization and in vitro properties of anti-bacterial Ag-based bioceramic coatings formed on zirconium by micro arc oxidation and thermal evaporation. *Surf. Coat. Technol.* **331**, 107–115. https://doi.org/10.1016/j.surfcoat.2017.10.023 (2017).
10. Fidan, S. *et al.* Fabrication of oxide layer on zirconium by micro-arc oxidation: Structural and antimicrobial characteristics. *Mater. Sci. Eng. C Mater. Biol. Appl.* **71**, 565–569. https://doi.org/10.1016/j.msec.2016.11.035 (2017).
11. Violant, D., Galofre, M., Nart, J. & Teles, R. P. In vitro evaluation of a multispecies oral biofilm on different implant surfaces. *Biomed. Mater.* **9**, 035007. https://doi.org/10.1088/1748-6041/9/3/035007 (2014).
12. D'Ercole, S., Piattelli, A., Marzo, G., Scarano, A. & Tripodi, D. Influence of bacterial colonization of the healing screws on peri-implant tissue. *J. Dent. Sci.* **8**, 109–114. https://doi.org/10.1016/j.jds.2012.12.012 (2013).

13. Alsaran, A. *et al.* Hydroxyapatite production on ultrafine-grained pure titanium by micro-arc oxidation and hydrothermal treatment. *Surf. Coat. Technol.* **205**, S537–S542. https://doi.org/10.1016/j.surfcoat.2011.03.032 (2011).
14. Kung, K. C., Lee, T. M. & Lui, T. S. Bioactivity and corrosion properties of novel coatings containing strontium by micro-arc oxidation. *J. Alloys Compd.* **508**, 384–390. https://doi.org/10.1016/j.jallcom.2010.08.057 (2010).
15. Yan, Y. Y., Han, Y., Li, D. C., Huang, J. J. & Lian, Q. Effect of $NaAlO_2$ concentrations on microstructure and corrosion resistance of Al_2O_3/ZrO2 coatings formed on zirconium by micro-arc oxidation. *Appl. Surf. Sci.* **256**, 6359–6366. https://doi.org/10.1016/j.apsusc.2010.04.017 (2010).
16. Lai, P. *et al.* Effect of micro-arc oxidation on fretting wear behavior of zirconium alloy exposed to high temperature water. *Wear* **424**, 53–61. https://doi.org/10.1016/j.wear.2019.02.001 (2019).
17. Matykina, E. *et al.* Plasma electrolytic oxidation of a zirconium alloy under AC conditions. *Surf. Coat. Technol.* **204**, 2142–2151. https://doi.org/10.1016/j.surfcoat.2009.11.042 (2010).
18. Yerokhin, A. L., Nie, X., Leyland, A., Matthews, A. & Dowey, S. J. Plasma electrolysis for surface engineering. *Surf. Coat. Technol.* **122**, 73–93. https://doi.org/10.1016/s0257-8972(99)00441-7 (1999).
19. Cheng, Y., Matykina, E., Arrabal, R., Skeldon, P. & Thompson, G. E. Plasma electrolytic oxidation and corrosion protection of Zircaloy-4. *Surf. Coat. Technol.* **206**, 3230–3239. https://doi.org/10.1016/j.surfcoat.2012.01.011 (2012).
20. Asadi, A., Razavi, S., Talebi, M. & Gholami, M. A review on anti-adhesion therapies of bacterial diseases. *Infection* **47**, 13–23. https://doi.org/10.1007/s15010-018-1222-5 (2019).
21. Gristina, A. G., Hobgood, C. D., Webb, L. X. & Myrvik, Q. N. Adhesive colonization of biomaterials and antibiotic resistance. *Biomaterials* **8**, 423–426. https://doi.org/10.1016/0142-9612(87)90077-9 (1987).
22. Campoccia, D., Montanaro, L. & Arciola, C. R. The significance of infection related to orthopedic devices and issues of antibiotic resistance. *Biomaterials* **27**, 2331–2339. https://doi.org/10.1016/j.biomaterials.2005.11.044 (2006).
23. Struelens, M. J. & Denis, O. Methicillin resistant *Staphylococcus aureus*: Toward a coordinated response to a continuing challenge. *Euro Surveill.* **5**, 25–26 (2000).
24. Gold, H. S. & Moellering, R. C. Drug therapy—Antimicrobial-drug resistance. *N. Engl. J. Med.* **335**, 1445–1453. https://doi.org/10.1056/nejm199611073351907 (1996).
25. Mah, T. F. & O'Toole, G. A. Related articles, mechanisms of biofilm resistance to antimicrobial agents. *Trends Microbiol.* **9**, 34–39 (2001).
26. Schwank, S., Rajacic, Z., Zimmerli, W. & Blaser, J. Impact of bacterial biofilm formation on in vitro and in vivo activities of antibiotics. *Antimicrob. Agents Chemother.* **42**, 895–898. https://doi.org/10.1128/aac.42.4.895 (1998).
27. Konig, C., Schwank, S. & Blaser, J. Factors compromising antibiotic activity against biofilms of *Staphylococcus epidermidis*. *Eur. J. Clin. Microbiol. Infect. Dis.* **20**, 20–26 (2001).
28. Battocchio, C. *et al.* Chitosan functionalization of titanium and Ti6Al4V alloy with chloroacetic acid as linker agent. *Mater. Sci. Eng. C Mater. Biol. Appl.* **99**, 1133–1140. https://doi.org/10.1016/j.msec.2019.02.052 (2019).
29. Li, B. *et al.* Biological and antibacterial properties of the micro-nanostructured hydroxyapatite/chitosan coating on titanium. *Sci. Rep.* https://doi.org/10.1038/s41598-019-49941-0 (2019).
30. Cremar, L. *et al.* Development of antimicrobial chitosan based nanofiber dressings for wound healing applications. *Nanomed. J.* **5**, 6–14. https://doi.org/10.22038/nmj.2018.05.002 (2018).
31. Santos, V. P. *et al.* Seafood waste as attractive source of chitin and chitosan production and their applications. *Int. J. Mol. Sci.* **21**, 4290. https://doi.org/10.3390/ijms21124290 (2020).
32. Li, J. H. & Zhuang, S. L. Antibacterial activity of chitosan and its derivatives and their interaction mechanism with bacteria: Current state and perspectives. *Eur. Polym. J.* **138**, 109984. https://doi.org/10.1016/j.eurpolymj.2020.109984 (2020).
33. Liu, H., Du, Y. M., Wang, X. H. & Sun, L. P. Chitosan kills bacteria through cell membrane damage. *Int. J. Food Microbiol.* **95**, 147–155. https://doi.org/10.1016/j.ijfoodmicro.2004.01.022 (2004).
34. Krajewska, B., Wydro, P. & Janczyk, A. Probing the modes of antibacterial activity of chitosan. Effects of pH and molecular weight on chitosan interactions with membrane lipids in Langmuir films. *Biomacromol* **12**, 4144–4152. https://doi.org/10.1021/bm2012295 (2011).
35. Raafat, D., von Bargen, K., Haas, A. & Sahl, H. G. Insights into the mode of action of chitosan as an antibacterial compound. *Appl. Environ. Microbiol.* **74**, 3764–3773. https://doi.org/10.1128/aem.00453-08 (2008).
36. Chung, Y. C. & Chen, C. Y. Antibacterial characteristics and activity of acid-soluble chitosan. *Bioresour. Technol.* **99**, 2806–2814. https://doi.org/10.1016/j.biortech.2007.06.044 (2008).
37. Yu, W. Z. *et al.* Synergistic antibacterial activity of multi components in lysozyme/chitosan/silver/hydroxyapatite hybrid coating. *Mater. Des.* **139**, 351–362. https://doi.org/10.1016/j.matdes.2017.11.018 (2018).
38. Schaechter, M. *Aging, Carcinogenesis, and Radiation Biology* 1–10 (Springer, 1976).
39. Wang, Z. S. *et al.* Microarc-oxidized titanium surfaces functionalized with microRNA-21-loaded chitosan/hyaluronic acid nanoparticles promote the osteogenic differentiation of human bone marrow mesenchymal stem cells. *Int. J. Nanomed.* **10**, 6675. https://doi.org/10.2147/ijn.S94689 (2015).
40. Neupane, M. P., Park, I. S. & Lee, M. H. Surface characterization and corrosion behavior of micro-arc oxidized Ti surface modified with hydrothermal treatment and chitosan coating. *Thin Solid Films* **550**, 268–271. https://doi.org/10.1016/j.tsf.2013.11.008 (2014).
41. Fang, K. X. *et al.* Immobilization of chitosan film containing semaphorin 3A onto a microarc oxidized titanium implant surface via silane reaction to improve MG63 osteogenic differentiation. *Int. J. Nanomed.* **9**, 4649–4657. https://doi.org/10.2147/ijn.S68895 (2014).
42. Zhang, J. *et al.* Degradable behavior and bioactivity of micro-arc oxidized AZ91D Mg alloy with calcium phosphate/chitosan composite coating in m-SBF. *Colloids Surf. B Biointerfaces* **111**, 179–187. https://doi.org/10.1016/j.colsurfb.2013.05.040 (2013).
43. Liu, P., Pan, X., Yang, W. H., Cai, K. Y. & Chen, Y. S. Improved anticorrosion of magnesium alloy via layer-by-layer self-assembly technique combined with micro-arc oxidation. *Mater. Lett.* **75**, 118–121. https://doi.org/10.1016/j.matlet.2012.02.016 (2012).
44. Cheng, S., Wei, D. Q. & Zhou, Y. Structure of microarc oxidized coatings containing Si, Ca and Na on titanium and deposition of cefazolin sodium/chitosan composite film. *Surf. Coat. Technol.* **205**, 3798–3804. https://doi.org/10.1016/j.surfcoat.2011.01.042 (2011).
45. Bai, K. F. *et al.* Fabrication of chitosan/magnesium phosphate composite coating and the in vitro degradation properties of coated magnesium alloy. *Mater. Lett.* **73**, 59–61. https://doi.org/10.1016/j.matlet.2011.12.102 (2012).
46. Yu, C. *et al.* Self-degradation of micro-arc oxidation/chitosan composite coating on Mg-4Li-1Ca alloy. *Surf. Coat. Technol.* **344**, 1–11. https://doi.org/10.1016/j.surfcoat.2018.03.007 (2018).
47. Aktug, S. L., Durdu, S., Yalcin, E., Cavusoglu, K. & Usta, M. Bioactivity and biocompatibility of hydroxyapatite-based bioceramic coatings on zirconium by plasma electrolytic oxidation. *Mater. Sci. Eng. C Mater. Biol. Appl.* **71**, 1020–1027. https://doi.org/10.1016/j.msec.2016.11.012 (2017).
48. Aktug, S. L., Durdu, S., Yalcin, E., Cavusoglu, K. & Usta, M. In vitro properties of bioceramic coatings produced on zirconium by plasma electrolytic oxidation. *Surf. Coat. Technol.* **324**, 129–139. https://doi.org/10.1016/j.surfcoat.2017.05.069 (2017).
49. Kokubo, T. & Takadama, H. How useful is SBF in predicting in vivo bone bioactivity?. *Biomaterials* **27**, 2907–2915. https://doi.org/10.1016/j.biomaterials.2006.01.017 (2006).

50. Sandhyarani, M., Rameshbabu, N., Venkateswarlu, K. & Krishna, L. R. Fabrication, characterization and in-vitro evaluation of nanostructured zirconia/hydroxyapatite composite film on zirconium. *Surf. Coat. Technol.* **238**, 58–67. https://doi.org/10.1016/j.surfcoat.2013.10.039 (2014).
51. Aktug, S. L., Kutbay, I. & Usta, M. Characterization and formation of bioactive hydroxyapatite coating on commercially pure zirconium by micro arc oxidation. *J. Alloys Compd.* **695**, 998–1004. https://doi.org/10.1016/j.jallcom.2016.10.217 (2017).
52. Kokubo, T., Kim, H. M. & Kawashita, M. Novel bioactive materials with different mechanical properties. *Biomaterials* **24**, 2161–2175. https://doi.org/10.1016/s0142-9612(03)00044-9 (2003).
53. Theunissen, G. S. A. M., Winnubst, A. J. A. & Burggraaf, A. J. Effect of dopants on the sintering behaviour and stability of tetragonal zirconia ceramics. *J. Eur. Ceram. Soc.* **9**, 251–263. https://doi.org/10.1016/0955-2219(92)90060-Q (1992).
54. Nayak, Y., Rana, R., Pratihar, S. & Bhattacharyya, S. Low-temperature processing of dense hydroxyapatite–zirconia composites. *Int. J. Appl. Ceram. Technol.* **5**, 29–36. https://doi.org/10.1111/j.1744-7402.2008.02180.x (2008).
55. Rapacz-Kmita, A., Paluszkiewicz, C., Slosarczyk, A. & Paszkiewicz, Z. FTIR and XRD investigations on the thermal stability of hydroxyapatite during hot pressing and pressureless sintering processes. *J. Mol. Struct.* **744**, 653–656. https://doi.org/10.1016/j.molstruc.2004.11.070 (2005).
56. Halada, G. *et al.* in *Biomaterials* Vol. 1054 *ACS Symposium Series* (eds A. S. Kulshrestha, A. Mahapatro, & L. A. Henderson) 159–171 (2010).
57. Sun, T., Wu, C. L., Hao, H., Dai, Y. & Li, J. R. Preparation and preservation properties of the chitosan coatings modified with the in situ synthesized nano SiO_x. *Food Hydrocolloids* **54**, 130–138. https://doi.org/10.1016/j.foodhyd.2015.09.019 (2016).
58. Wu, C. S., Hsu, Y. C., Liao, H. T. & Cai, Y. X. Antibacterial activity and in vitro evaluation of the biocompatibility of chitosan-based polysaccharide/polyester membranes. *Carbohydr. Polym.* **134**, 438–447. https://doi.org/10.1016/j.carbpol.2015.08.021 (2015).
59. Zhang, Y. *et al.* Preparation of beta-$Ca_3(PO_4)_2$ bioceramic powder from calcium carbonate and phosphoric acid. *Curr. Appl. Phys.* **5**, 531–534. https://doi.org/10.1016/j.cap.2005.01.026 (2005).
60. Sogias, I. A., Khutoryanskiy, V. V. & Williams, A. C. Exploring the factors affecting the solubility of chitosan in water. *Macromol. Chem. Phys.* **211**, 426–433. https://doi.org/10.1002/macp.200900385 (2010).
61. Zhang, F. *et al.* Preparation of superhydrophobic films on titanium as effective corrosion barriers. *Appl. Surf. Sci.* **257**, 2587–2591. https://doi.org/10.1016/j.apsusc.2010.10.027 (2011).
62. Farris, S. *et al.* Wetting of biopolymer coatings: Contact angle kinetics and image analysis investigation. *Langmuir* **27**, 7563–7574. https://doi.org/10.1021/la2017006 (2011).
63. Bangyekan, C., Aht-Ong, D. & Srikulkit, K. Preparation and properties evaluation of chitosan-coated cassava starch films. *Carbohydr. Polym.* **63**, 61–71. https://doi.org/10.1016/j.carbpol.2005.07.032 (2006).
64. Durdu, S., Usta, M. & Berkem, A. S. Bioactive coatings on Ti6Al4V alloy formed by plasma electrolytic oxidation. *Surf. Coat. Technol.* **301**, 85–93. https://doi.org/10.1016/j.surfcoat.2015.07.053 (2016).
65. Bayrak, G. K., Demirtas, T. T. & Gumusderelioglu, M. Microwave-induced biomimetic approach for hydroxyapatite coatings of chitosan scaffolds. *Carbohydr. Polym.* **157**, 803–813. https://doi.org/10.1016/j.carbpol.2016.10.016 (2017).
66. Gross, K. A. & Berndt, C. C. In vitro testing of pasma sprayed hydroxyapatite coatings. *J. Mater. Sci. Mater. Med.* **5**, 219–224 (1994).
67. Schiffman, J. D. & Schauer, C. L. Solid state characterization of alpha-chitin from *Vanessa cardui* Linnaeus wings. *Mater. Sci. Eng. C Biomim. Supramol. Syst.* **29**, 1370–1374. https://doi.org/10.1016/j.msec.2008.11.006 (2009).
68. Subhapradha, N. *et al.* Physicochemical characterisation of beta-chitosan from *Sepioteuthis lessoniana* gladius. *Food Chem.* **141**, 907–913. https://doi.org/10.1016/j.foodchem.2013.03.098 (2013).
69. Lopez-Mata, M. A. *et al.* Physicochemical and antioxidant properties of chitosan films incorporated with cinnamon oil. *Int. J. Polym. Sci.* https://doi.org/10.1155/2015/974506 (2015).
70. Si Trung, T. & Bao, H. N. Physicochemical properties and antioxidant activity of chitin and chitosan prepared from pacific white shrimp waste. *Int. J. Carbohydr. Chem.* **2015**, 1–6 (2015).
71. Raafat, D. & Sahl, H. G. Chitosan and its antimicrobial potential—A critical literature survey. *Microb. Biotechnol.* **2**, 186–201. https://doi.org/10.1111/j.1751-7915.2008.00080.x (2009).
72. Monarul Islam, M. D., Masum, M. S. D. & Mahbub, K. R. In vitro antibacterial activity of shrimp chitosan against *Salmonella paratyphiand Staphylococcus aureus*. *J. Bangladesh Chem. Soc.* **24**, 185–190 (2011).
73. Zhang, X. D. *et al.* Preparation of chitosan-TiO_2 composite film with efficient antimicrobial activities under visible light for food packaging applications. *Carbohydr. Polym.* **169**, 101–107. https://doi.org/10.1016/j.carbpol.2017.03.073 (2017).
74. Munteanu, B. S. *et al.* Chitosan coatings applied to polyethylene surface to obtain food-packaging materials. *Cellul. Chem. Technol.* **48**, 565–575 (2014).
75. Chung, Y. C. *et al.* Relationship between antibacterial activity of chitosan and surface characteristics of cell wall. *Acta Pharmacol. Sin.* **25**, 932–936 (2004).
76. Masson, M. *et al.* Antimicrobial activity of piperazine derivatives of chitosan. *Carbohydr. Polym.* **74**, 566–571. https://doi.org/10.1016/j.carbpol.2008.04.010 (2008).
77. Esmaeili, A. & Ghobadianpour, S. Vancomycin loaded superparamagnetic $MnFe_2O_4$ nanoparticles coated with PEGylated chitosan to enhance antibacterial activity. *Int. J. Pharm.* **501**, 326–330. https://doi.org/10.1016/j.ijpharm.2016.02.013 (2016).

Acknowledgements

The authors would like to special thank Prof. Emine Yalcin for helping bacterial tests at Giresun University and Mr. Ilhan Irende for running SEM and EDS analyses at ODUMARAL.

Author contributions

S.L.A. prepared Zr samples and fabricated the MAO coatings. S.D. carried out some experiments such as FTIR, SEM-EDX, contact angle measurements, in vitro SBF immersion tests and XRD anaysis at post-immersion SBF. S.K. coated chitosan layer on the MAO coated Zr surfaces. K.C. carries out in vitro antibacterial tests. M.U. carried out XRD analysis on the MAO surfaces. S.L.A., S.D., S.K., K.C. and M.U. wrote manuscript text. S.D. prepared Figs. 1, 2, 3, 4, 5, 6, 7 and 8 and Tables 1 and 2. K.C. prepared Fig. 9. All authors reviewed the manuscript.

Competing interests

The authors declare no competing interests.

Additional information

Correspondence and requests for materials should be addressed to M.U.

Reprints and permissions information is available at www.nature.com/reprints.